Performance Characterization of ESA's Tropospheric Delay Calibration System for Advanced Radio Science Experiments

Riccardo Lasagni Manghi[1], Marco Zannoni[1,2], Paolo Tortora[1,2], Antonio Martellucci[3], Javier De Vicente[4], Jose Villalvilla[4], Mattia Mercolino[4], Gerrit Maschwitz[5], Thomas Rose[5]

[1]Alma Mater Studiorum - Università di Bologna, Dipartimento di Ingegneria Industriale, Forlì, Italy
[2] Alma Mater Studiorum - Università di Bologna, Centro Interdipartimentale di Ricerca Industriale Aerospaziale, Forlì, Italy
[3]European Space Agency, ESA-ESTEC, Noordwijk, Netherlands
[4]European Space Agency, ESA-ESOC, Darmstadt, Germany
[5]RPG Radiometer Physics GmbH, Meckenheim, Germany

Corresponding author: Riccardo Lasagni Manghi (riccardo.lasagni@unibo.it)

Key Points:

- A prototype water vapor radiometer for tropospheric delay calibration was installed at the Deep Space Antenna complex in Malargüe.
- The instrument performance has been statistically characterized through orbit determination of the Gaia spacecraft.
- Our results indicate that the instrument allows for improved frequency stability with respect to current calibrations.

Abstract

Media propagation noises are amongst the main error sources of radiometric observables for deep space missions, with fluctuations of the tropospheric excess path length representing a relevant contributor to the Doppler noise budget. Microwave radiometers currently represent the most accurate instruments for the estimation of the tropospheric path delay (or excess path length) along a slant direction. A prototype of a Tropospheric Delay Calibration System (TDCS), using a 14 channel K_a/V band microwave radiometer, has been developed under ESA contract and installed at the deep-space antenna DS3 complex in Malargüe (Argentina) in February 2019. After its commissioning, the TDCS has been involved in an extensive testbed campaign by recording a total of 44 tracking passes of the Gaia spacecraft, which were used to perform an orbit determination analysis. This work presents the first statistical characterization of the end-to-end performance of the TDCS prototype in an operational scenario. The results show that using TDCS-based calibrations instead of the standard GNSS-based calibrations leads to a significant reduction of the residual Doppler noise and instability.

1 Introduction

Precise radiometric tracking is of key importance during operations of interplanetary missions and for advanced radio science applications. Radio science research performed on deep space missions like Cassini, BepiColombo, and the upcoming JUICE mission, rely on a combination of X and K_a band radio links to mitigate the dispersive effects of propagation through interplanetary plasma, solar corona and Earth ionosphere, leaving tropospheric delay as one of the main error contributors to Doppler and ranging measurements.

To meet the demanding requirements of BepiColombo's Mercury Orbiter Radio science Experiment (MORE) (Iess, et al., 2021) and JUICE's Geodesy and Geophysics of Jupiter and the Galilean Moons (3GM) (Cappuccio, et al., 2020) Radio Science experiment, in terms of radiometric tracking accuracy and end-to-end stability of the Doppler signals, ground-based Microwave Radiometers (MWR) are deemed as the most appropriate instruments for tropospheric delay calibration (Iess, Asmar, & Tortora, 2009).

The use of MWRs to calibrate the tropospheric delay for deep space tracking was originally introduced by JPL to support the Cassini radio science experiments (Naudet, et al., 2000), (Resch, et al., 2001), (Tanner & Riley, 2003). In the following years, in combination with multi-frequency links to calibrate the dispersive media, such as the ones available on Cassini and Juno, the use of a MWR allowed to reach a remarkable end-to-end fractional frequency stability, expressed in terms of Allan Standard Deviation (ASD), of about 1×10^{-14} at a 1000 s stability interval (Tortora, Iess, Bordi, Ekelund, & Roth, 2004), (Durante, et al., 2020). Later, ESA performed a preliminary study named AWARDS (Tortora, et al., 2013), (Graziani, et al., 2014) for the definition of the requirements and preliminary system design of a Tropospheric Delay Calibration system (TDCS). In addition, media calibration performance requirements for accurate spacecraft (S/C) tracking were studied in detail in another ESA study called ASTRA (Iess, et al., 2012) (Iess, et al., 2014).

The TDCS described here represents the prototype of a new instrument for the calibration of tropospheric delay based on a high stability and high accuracy K_a/V band MWR, which was developed in the framework of an ESA-ESTEC contract by a consortium formed by Radiometer Physics GmbH (RPG), University of Bologna, and the Université Catholique de Louvain.

Specifically, this work focuses on the end-to-end performance characterization of the TDCS system, which was carried out through a detailed orbit determination (OD) analysis of Doppler measurements acquired during several tracking passes of ESA's Gaia S/C.

It is important to clarify that the purpose of this test is not to reproduce the full OD solution used for the navigation of Gaia, but to validate the TDCS products by making a punctual evaluation of the relative end-to-end noise reduction when TDCS-based calibrations are used in place of standard GNSS-based calibrations.

2 Tropospheric Delay Calibration System

The TDCS is a combination of instruments, software (S/W) tools and operational procedures that allows an accurate estimation of the tropospheric delay along the slant direction while minimizing the effect of the instrument instability. The main TDCS subsystem is an ultra-stable MWR for deep-space applications, which represents a modified version of the standard HATPRO-G5 MWR developed by RPG (Maschwitz, Czekala, Orlandi, & Rose, 2019). A description of the concept and design of the first HATPRO generation is given by Rose, et al. (2005). In 2015, the radiometric performance was significantly improved with the fifth generation of the series (G5). The TDCS, shown in Figure 1, measures sky noise emissions at frequencies near the water vapor absorption peak at 22.2 GHz, the oxygen absorption band around 60 GHz and in the 30 GHz window, which is sensitive to liquid water content (clouds and rain). With respect to the standard HATPRO-G5 RpG radiometer, this instrument was tailored for S/C tracking applications by adding: a) a 2-axes Antenna Tracking System (ATS) to gain full sky scanning capabilities; b) a modified antenna system including an external heated parabolic reflector, which narrows the MWR half-power beamwidth down to 1.2°, allowing to better replicate the air volume sampled by the Deep Space Antenna (DSA) and to reduce the effect of solar radiation contamination during periods of superior conjunction; c) a high precision meteo station providing values of air pressure, temperature, relative humidity, rain rate and wind at ground level. The instrument includes internal and external temperature control and antenna blower systems to avoid water condensation and icing on the exposed surfaces and to maintain accurate stability of the receivers' temperature.
Further updates include new control procedures for the ATS, specific calibration procedures for the instrument parameters, and the development of an external S/W tool that acts as a high-level access point for monitoring and controlling of the TDCS functions by the ground station Front-End Controller (FEC).

Figure 1 The TDCS prototype deployed at ESA's DS3 complex in Malargüe, Argentina.

3 Testbed summary and data availability

Two successive testbed campaigns were carried out between February and July 2019, targeting a total of 44 tracking passes of ESA's Gaia S/C. Both H/W and S/W updates were performed in response to issues that were encountered during the test campaign. As a result, availability of key data products (Doppler data, GNSS-based calibrations, and TDCS-based calibrations) has varied among the different tracking passes. Since the simultaneous availability of all these products is required for the performance evaluation, only 32 of the total passes were eventually included within the OD analysis, as shown in Table 1, which provides an overview of this subset along with a summary of the atmospheric conditions that were encountered during each pass.

The range of TDCS retrieved ZWD values provides an indication of the potential improvement that can be obtained when tropospheric calibrations are introduced in the OD process. Being Gaia only visible at night, most of the tracking passes are characterized by dry conditions, which can limit the effectiveness of the TDCS calibrations. Values of TDCS retrieved Liquid Water Path (LWP) above ~10 g/m^2 indicate the presence of condensed water (clouds or fog) along the TDCS line-of-sight. These values scale with the length of the propagation path through the cloud, so high LWP values (i.e.~ 500-1000 g/m^2) indicate the presence of thick cloud formations and may suggest the presence of precipitated water, in particular when coupled with the triggering of the Rain Flag (RF) by the rain sensor included within the TDCS. Characteristic integrated values for wind speed (WS) and turbulence strength (C_N^2), derived from the European Center for Medium Weather Forecast (ECMWF) database (Molteni, Buizza, Palmer, & Petroliagis, 1996), can be considered as proxy parameters for the presence of turbulent eddies in the lower portions of the atmosphere, which affect the accuracy of the TDCS calibrations (Lasagni Manghi, et al., 2019). Both values of WS and C_N^2 were provided by UCL (Quibus, et al., 2019) and were derived by averaging over time the local vertical profiles from the ECMWF dataset that fell within the tracking pass interval, when available. The obtained vertical profiles were then spatially averaged from ground level to a height of 1 km above the surface.

Finally, the wind speed at ground level, measured by the TDCS meteo station, provides on one hand an indication of the strength of the mechanical noise introduced in the Doppler measurements by the tropospheric calibrations, and on the other hand represents another proxy for the effect of wind shears on tropospheric turbulence.

Table 1 Summary of data availability and main meteorological parameters for the analyzed tracking passes: a) pass ID number; b) date; c) time coverage; d) characteristic elevations, corresponding to the start of the session, the maximum value, and the end of the session, respectively; e) Boolean indicating the activation of the rain flag of the TDCS meteo station; f) 99th percentile of the estimated LWP along the slant direction; g) range of estimated ZWD values; h) 99th percentile of the wind speed measured by the TDCS meteo station; i) characteristic integrated wind speed derived from the ECMWF dataset; j) characteristic integrated turbulence strength derived from the ECMWF dataset.

Pass ID	Date	From/To	El [°]	RF	LWP [g/m^2]	ZWD [mm]	WS_{TDCS} [km/h]	WS_{ECMWF} [km/h]	C_N^2 [km/h]
1	16 February 2019	[02:00, 03:30]	[27, 37, 37]	NO	62	[99, 104]	10	-	-
2	17 February 2019	[02:00, 03:30]	[27, 37, 37]	NO	281	[132, 155]	15	-	-
3	23 February 2019	[02:00, 03:30]	[26, 38, 38]	NO	24	[112, 121]	8	-	-
4	24 February 2019	[02:00, 03:30]	[26, 38, 38]	NO	18	[24, 32]	25	-	-
5	25 February 2019	[08:00, 09:30]	[26, 26, 15]	NO	106	[55, 61]	30	-	-
6	26 February 2019	[08:00, 09:30]	[27, 27, 15]	NO	83	[46, 49]	8	-	-
7	27 February 2019	[01:00, 03:30]	[15, 39, 39]	YES	32	[75, 83]	11	-	-
8	03 March 2019	[01:30, 03:30]	[15, 40, 40]	NO	36	[75, 87]	8	-	-
9	09 April 2019	[02:00, 11:00]	[21, 62, 15]	NO	136	[46, 66]	14	9.86	$5.34 \cdot 10^{-14}$
10	10 April 2019	[00:00, 11:00]	[20, 62, 15]	YES	141	[59, 78]	30	19.75	$5.75 \cdot 10^{-14}$
11	11 April 2019	[02:00, 11:00]	[22, 62, 15]	NO	145	[47, 71]	6	29.11	$4.14 \cdot 10^{-14}$

12	12 April 2019	[00:00, 10:00]	[15, 62, 19]	NO	142	[38, 70]	10	18.53	$1.27 \cdot 10^{-13}$
13	14 April 2019	[02:00, 11:00]	[23, 63, 15]	NO	106	[14, 26]	42	42.61	$7.83 \cdot 10^{-14}$
14	16 April 2019	[01:00, 08:30]	[24, 64, 36]	NO	47	[51, 67]	10	20.27	$1.60 \cdot 10^{-13}$
15	17 April 2019	[02:00, 08:30]	[24, 64, 36]	NO	23	[28, 45]	13	23.16	$4.90 \cdot 10^{-14}$
16	18 April 2019	[00:00, 10:30]	[15, 65, 18]	NO	85	[53, 71]	8	22.49	$7.82 \cdot 10^{-14}$
17	19 April 2019	[00:00, 10:00]	[15, 65, 28]	NO	262	[63, 104]	27	16.87	$9.19 \cdot 10^{-14}$
18	20 April 2019	[00:00, 09:30]	[15, 65, 32]	YES	2555	[85, 172]	9	16.34	$4.83 \cdot 10^{-14}$
19	21 April 2019	[00:00, 08:30]	[15, 66, 43]	NO	79	[60, 73]	10	17.79	$8.73 \cdot 10^{-14}$
20	22 April 2019	[00:00, 07:30]	[15, 66, 52]	NO	69	[64, 75]	9	20.91	$5.66 \cdot 10^{-14}$
21	23 April 2019	[01:00, 08:30]	[15, 66, 41]	NO	43	[74, 97]	8	5.37	$1.40 \cdot 10^{-14}$
22	29 April 2019	[23:30[1], 07:30]	[15, 69, 51]	NO	134	[48, 97]	15	28.16	$9.18 \cdot 10^{-14}$
23	30 April 2019	[01:00, 06:00]	[19, 69, 66]	NO	405	[69, 84]	8	16.24	$6.22 \cdot 10^{-14}$
24	01 May 2019	[23:30[1], 05:00]	[15, 69, 69]	NO	128	[27, 61]	15	24.77	$1.35 \cdot 10^{-13}$
25	04 May 2019	[23:30[1], 05:00]	[15, 70, 70]	NO	1082	[100, 127]	12	15.61	$3.02 \cdot 10^{-14}$
26	11 May 2019	[23:00[1], 03:00]	[15, 62, 62]	NO	141	[32, 47]	10	15.21	$7.77 \cdot 10^{-14}$
27	19 May 2019	[23:00[1], 06:00]	[15, 75, 66]	NO	183	[54, 71]	8	15.31	$7.65 \cdot 10^{-14}$
28	29 June 2019	[21:30[1], 05:30]	[15, 83, 64]	NO	36	[54, 71]	13	26.73	$6.65 \cdot 10^{-14}$
29	30 June 2019	[21:30[1], 06:00]	[21, 83, 61]	NO	25	[22, 47]	25	33.08	$6.02 \cdot 10^{-14}$
30	11 July 2019	[06:30, 09:00]	[53, 53, 25]	NO	2	[28, 38]	10	-	-
31	16 July 2019	[06:00, 09:00]	[63, 63, 20]	NO	1	[41, 46]	12	18.36	$1.19 \cdot 10^{-13}$
32	18 July 2019	[07:00, 09:00]	[47, 47, 20]	NO	0	[52, 74]	23	-	-

4 TDCS data processing

The retrieval of atmospheric variables from MWR observations is an ill-posed problem, since a given set of Brightness Temperature (TB) measurements may be related to several different atmospheric states (Keihm & Marsh, 1998). To resolve this ambiguity, the TDCS uses a Neural Network (NN) retrieval algorithm, which was trained using a large number of atmospheric vertical profiles extracted specifically for the Malargüe site from a numerical weather prediction model (ECMWF reanalysis). From each of these profiles of temperature, humidity, pressure and liquid water concentration, the Slant Wet Delay (SWD) was computed. At the same time, each profile was used as input for the simulation of the corresponding TB measurements via a state-of-the art radiative transfer model. The resulting dataset was split into a training part and a test part. For the former, pairs of simulated TB measurements and SWD values were used to derive a set of retrieval coefficients, which minimized the SWD output error over the complete training dataset. The latter served for validation of the retrieval performance through a statistical comparison of SWD values calculated from the test profiles and the SWD values retrieved via the NN coefficients.

During operations, the retrieval coefficients related the measured TB input vector (14 K_a/V band channels) to the best SWD value. Since TB measurements and SWD scale differently with the length of the propagation path through the atmosphere, the estimation process of the retrieval parameters was repeated at 19 discrete elevation angles (spaced at constant airmass steps) covering the range between 10° and 90°, leading to the generation of an elevation-dependent grid of retrieval coefficients. The discrete angle-grid may cause artificial effects at low elevation angles (<30°). This was handled by a smart interpolation scheme based on the following steps: at first, the mean radiative temperature (TMR) was derived from surface sensors observations and a dedicated NN retrieval and used to derive the atmospheric opacity from TB values. Then, the atmospheric opacity was linearly interpolated to the nearest nodes on the SWD retrieval grid and used to derive the corresponding TB values using TMR, neglecting the small variation of TMR with airmass. Finally,

[1] The start times for these OD passes correspond to the previous day with respect to the date reported in the 2nd column.

the SWD output was calculated as an airmass weighted average of the SWD values retrieved for the two considered grid nodes.
For each of the analyzed tracking passes, SWD values were retrieved from TB measurements using the trained NN retrieval and converted to Zenith Wet Delay (ZWD) using a sin(*el*) mapping function, where *el* represents the instantaneous elevation as indicated by the ATS. This simple mapping was preferred to higher fidelity mapping functions, such as the one from Niell (1996), to be consistent with the procedures used for the NN retrieval training.
Then, ZWD outliers were identified and removed using a z-score technique to evaluate the deviation of each data point from a smoothed dataset, which was generated using a median filter with a 10 minute time window.
Finally, Control Statement Processor (CSP) calibration cards were generated from the ZWD time series using a linear piecewise fit between consecutive data points and according to the definitions in (TRK-2-23 Media Calibration Interface, 2008). Several CSP cards were generated with increasing values of the ZWD integration time to improve the signal-to-noise ratio. Specifically, TDCS calibrations with 1 s, 20 s, and 60 s integration time for the ZWD time series were respectively used and compared within the OD analysis .

The Zenith Hydrostatic Delay (ZHD) was computed according to the model of Saastamoinen (1971), using equation (4.1). In this expression, p_S [hPa] is the surface pressure measured by the TDCS meteo sensor, λ [°] is the geocentric latitude, and h [m] is the height over the Mean Sea Level (MSL). Coordinates for the TDCS and DSA phase center are provided in Table 2.

$$ZHD = 2.2767 \cdot 10^{-3} \frac{p_S}{1 - 0.0266 \cdot \cos(2\lambda) - 0.00028 \cdot h} \ [m] \tag{4.1}$$

The ZHD values were scaled to the height of the phase center of the DSA using the correction provided in equation (4.2), where Δh [m] is the height difference between the TDCS and the DSA phase center, p_S [hPa] is the surface pressure, and T_S [K] is the surface temperature. This expression is a modified version of the one from Estefan & Sovers (1994), where the average pressure and temperature of the vertical air column were replaced by the instantaneous surface measurements provided by the TDCS meteo station.

$$\Delta ZHD \cong -7.76 \cdot 10^{-5} \Delta h \frac{p_s}{T_s} \ [m] \tag{4.2}$$

The corrected ZHD values were then smoothed using a gaussian filter with a 10 minute time window and down-sampled to 20 s. This filtering process was required due to the limited resolution of data generated by the TDCS pressure sensor (0.1 hPa), which caused some discontinuities within the ZHD time series. These discontinuities had orders of magnitude similar to the short scale variations in the ZWD and might have resulted in an increased Doppler noise if not properly corrected. Finally, CSP calibration cards were generated from the ZHD time series using a linear piecewise fit between consecutive data points.

Table 2 Coordinates of the relevant GS instruments

	Latitude	Longitude	Height (MSL)
DSA	35° 46' 33.63" S	69° 23' 53.51" W	1571.5 [m]
TDCS	35° 46' 32.69" S	69° 23' 52.42" W	1552 [m]

5 Orbit Determination analysis

5.1 Introduction

Gaia is an ESA cornerstone scientific mission, whose aim is to measure the three-dimensional position and velocity distributions of stars within the Milky Way using accurate astrometric measurements (Prusti, De Brujine, Brown, & al., 2016). The selection of this particular mission for the TDCS testbed campaign was mainly driven by geometrical and operational considerations. Since Gaia operates from a Lissajous-type orbit around the second Earth-Sun Lagrange point (L_2), the S/C is constantly near solar opposition. This means that the impact of solar plasma and Earth ionosphere on the propagation delay is particularly limited, thus simplifying the processing and calibration procedures for the Doppler data. Furthermore, several Gaia tracking passes were already scheduled at the DS3 complex during the same time period, thus the inclusion of TDCS operations had a marginal impact on ground station operations.

The overall concept for this analysis was to perform a standard OD process for the Gaia S/C using Doppler measurements collected at DS3 and *a priori* information on the dynamical model provided by the Flight Dynamics team at ESA's European Space Operation Centre in Darmstadt, Germany (ESOC FD). This process was repeated by keeping all parameters fixed while varying the applied tropospheric calibrations (either generated from dual-frequency GNSS measurements or generated by the TDCS measurements) to allow for a direct comparison of the respective accuracies.

5.2 Data selection and processing

Raw Doppler measurements at X/X band acquired during the Gaia tracking passes between 16 February and 18 July 2019 were provided by ESA as collected by the Telemetry, Tracking and Command Processor (TTCP), according to the format definitions provided by Ricart (2018). As a first step, the set of Doppler observables was reduced by removing all measurements in the proximity of the chemically propelled maneuvers to avoid discontinuities.

Then, all observables collected below 15° of elevation at the ground station were removed to mitigate the progressive degradation of the radiometric retrieval accuracy. This value, which represents a conservative limit, was selected to account for the retrieval errors due to the granularity of the NN retrieval coefficients, possible fast variations of the observed atmospheric scene, and contaminations due to ground and clutter emission.

Doppler measurement weights for each tracking pass were computed as the root mean square (RMS) value of the residuals for that pass.

5.3 Media calibrations

For the most recent deep space missions, the dispersive effect from the charged particles in the solar corona is calibrated using a multi-frequency link with coherent up-link and down-link (Bertotti, Comoretto, & Iess, 1993) (Mariotti & Tortora, 2013). This was not possible for the current analysis, since Gaia uses a single frequency link at X-band. However, the effect of Solar plasma is assumed to be small, considering that the S/C operates near solar opposition, with Sun Earth Probe (SEP) angle values always larger than 170° (Asmar, Armstrong, Iess, & Tortora, 2005), (Iess, et al., 2014).

Another relevant source of propagation delay excess is represented by the dispersive effect of charged particles within the Earth's ionosphere. Radio Science and OD analyses mostly use ionospheric calibrations derived from GNSS dual-frequency measurements, which are provided in form of CSP cards. These data products are not routinely generated by ESOC FD, which relies instead on the analytical model of Jakowski, Hoque, & Mayer (2011) to estimate the Doppler and

ranging errors due to the Earth's ionosphere. The same approach was used for this analysis to generate a time series of corrections to be applied for the scheduled Gaia tracking passes. Being Gaia only visible at night, because of its solar opposition geometry, the ionospheric induced Doppler error at X-band was expected to be small when compared to the variations of tropospheric delay (Thornton & Border, 2003), as confirmed by the computed values, which were often below the 10 μm/s resolution of the Jakowsky model. Considering the small magnitude of these corrections and the limited resolution of the model, it was decided not to include the ionospheric calibrations within the final OD analysis, to avoid introducing discontinuities in the Doppler measurements.

5.4 Dynamical model

The overall goal of this analysis was to validate the TDCS products by performing a direct comparison between the OD performances obtained using TDCS-based calibrations and the ones obtained using standard GNSS-based calibrations. Keeping this in mind, the dynamical model was kept reasonably simple to reduce the likelihood of possible biases in the results caused by mismodelling errors

The gravitational accelerations that were considered for this analysis include point-mass gravity from the Sun, the planets and their satellites, the Moon, and Pluto. Higher order gravitational harmonics were neglected. State vectors and gravitational parameters for the Solar System bodies were taken from JPL's DE430 planetary ephemerides (Folkner, Williams, Boggs, Park, & Kuchynka, 2014).

Non-Gravitational Accelerations (NGA) were introduced in the form of interpolating polynomials using tabulated coefficients generated by ESOC FD, allowing for easier replicability. Specifically, the main NGAs acting on the S/C are the ones from Solar Radiation Pressure (SRP) and Thermal Radiation Pressure (TRP), which were provided in form of normalized acceleration components.

Gaia performed three main Orbit Trim Maneuvers (OTMs) throughout the testbed campaign: two station keeping OTMs, in February and April 2019, respectively, and an inclination change maneuver, split into 9 burns, in July 2019. All OTMs occurring during the tracking passes were modelled as impulsive burns and estimated within the filter using *a priori* ΔV values provided by ESOC FD.

Attitude control during chemically propelled maneuvers was performed using the Reaction Control System (RCS), which caused parasitic ΔVs to be imparted on the S/C. Similarly to the OTMs, RCS firings were modelled as impulsive burns and estimated within the filter.

Conversely, attitude control during standard operations was performed using a cold-gas Micro-Propulsion System (MPS), which caused parasitic accelerations to act permanently on the S/C. Instantaneous accelerations from cold-gas MPS thrusters were provided in tabulated form by ESOC FD.

5.5 Filter setup

The analysis was carried out using JPL's MONTE OD S/W (Evans et al., 2018), which adopts a weighted least-squares batch filter to generate iterative corrections to the *a priori* dynamical model in order to minimize the difference between the real and the simulated measurements (Bierman, 2006).

Table 3 summarizes the solve-for parameters within the square root information batch filter and their associated *a priori* uncertainties.

A priori values for the S/C state were taken from the operational trajectory reconstructed by ESOC FD. Another key parameter that was estimated within the filter is the phase center of the onboard

S/C antenna. Since Gaia uses two separate antennas for uplink and downlink, which are the Low-Gain Antenna (LGA1) and the Phased Array Antenna (PAA), respectively, the estimated antenna coordinates are actually referred to a virtual antenna (VA) located at the midpoint of the LGA1-PAA segment. Estimated values for the coordinates of the VA were consistent with the *a priori* uncertainty and mostly absorbed the short term variations in the location of the S/C center of mass. It should be noted that the VA coordinate along the spin axis, which corresponds to the x-axis of the S/C body frame, is not observable using Doppler measurements, so only the y and z components were estimated locally for each pass.

Table 3 Estimated parameters and their corresponding *a priori* uncertainties

Parameter	Type	N_{est}	*A priori* σ	Comments
S/C position	Local	3	100 km	*A priori* values were taken from the ESOC FD solution.
S/C velocity	Local	3	1 m/s	
VA position	Local	2	10 cm	*A priori* coordinates in the S/C body frame $x_{VA} \cong [-0.08, 0.775, -0.15]\ m$
ΔV (OTMs)	Global	$3\times N_{OTM}$	10 cm/s	*A priori* values were provided by ESOC FD
ΔV (RCS)	Global	$3\times N_{RCS}$	1 cm/s	

6 Results

The overall accuracy of the TDCS calibrations is driven by several intrinsic and scene-dependent factors. The former comprise all error sources which are related to the MWR components, such as the noise characteristics of the radiometric receivers, fluctuations of the absorption coefficient for the main reflector, and spill-over losses of the K_a band channels over a variable background. The latter comprise all error sources whose magnitude depends on the local atmospheric conditions encountered during the measurements. These include the retrieval error contribution, which depends on the completeness and variety of the training database, and a beam mismatch contribution related to the different air volumes observed by the TDCS and the DSA.

The impact of the radiometer noise performances and of the retrieval error on the calibration accuracy were the subject of previous investigations by the authors (Maschwitz, Czekala, Orlandi, & Rose, 2019), (Lasagni Manghi, et al., 2019), and were numerically quantified with simulations and testing in controlled environments. Analogously, the beam mismatch error was quantified by numerical simulations under specific atmospheric conditions (Graziani, et al., 2014).

When the tropospheric calibrations are included within the OD process, the Doppler measurements will thus be affected by a variable amount of uncalibrated (or residual) tropospheric delay and by additional error sources that are introduced as part of the calibration generation process.

Instead of focusing on individual error contributions, the current analysis provides an estimation of the end-to-end frequency stability of the Doppler residuals obtained when using either GNSS-based or TDCS-based tropospheric calibrations.

As a first step, a visual inspection of the Doppler residuals at 60 s count time was performed to highlight the presence of major signatures within the data and to identify possible causes for these features. The specific value of 60 s for the count time was selected since it represents a standard case for radio science applications (Tortora et al 2016, Durante et al 2019, Zannoni et al 2020, Gomez et al 2021). In fact, this value is sufficiently smaller than the characteristic time scales of the typical investigated processes and sufficiently large to avoid numerical noise issues (Zannoni and Tortora 2013). Absolute RMS values of the residuals were then produced for each pass, along with an estimation of the relative noise reduction between the two analyzed cases.

Finally, the overall stability of the Doppler residuals was quantified by computing the Allan Standard Deviation (ASD) according to equation (6.1), where y represents the normalized

frequency residuals, ΔT is the stability time interval, the brackets ⟨·⟩ indicate an ensemble average over the measured time series, and $\overline{y(t,\Delta T)}$ indicates a time average over the interval between t and t+ΔT, according to the expression in (6.2). Specifically, stability intervals of 20 s, 60 s, and 1000 s were considered, which represent typical values used for radio science applications.

$$ASD_y(\Delta T) = \left(\frac{\left\langle \left[\overline{y(t+\Delta T,\Delta T)} - \overline{y(t,\Delta T)} \right]^2 \right\rangle}{2} \right)^{1/2} \quad [\mathrm{s/s}] \tag{6.1}$$

$$\overline{y(t,\Delta T)} = \frac{1}{\Delta T} \int_t^{t+\Delta T} y(\tau)\, d\tau \tag{6.2}$$

In the following, a single representative pass is analyzed in detail according to the procedure described above. Then, a summary of all passes is produced with a quantitative comparison of the relative performances between the analyzed test cases.

6.1 Example tracking pass (19 April 2019)

This pass was selected as representative for standard conditions that were encountered at the DS3 complex in Malargüe. From Table 1, we observe that this pass was characterized by moderate liquid water content and that the rain flag was not triggered, suggesting the presence of clouds along the line of sight, with no precipitation. Moderate to high values of wind speed were also observed at ground level, in particular during the first hours of the pass. Vertical profiles from the ECMWF dataset also suggest the presence of moderate to high turbulence levels.

Figure 2 compares the Doppler residuals at 60 s count time, using GNSS-based calibrations (left) and TDCS-based calibrations, with 20 s integration time (right). With the introduction of TDCS calibrations we observe a consistent improvement in the residuals, with an overall 51% reduction of the RMS values and no apparent signature being introduced. The observed improvement is particularly pronounced during the first half of the tracking pass, where higher wind speed and LWP values are observed. This may provide an indication of the ability of the selected NN retrieval to correctly separate the information content of liquid water from the one provided by water vapor.

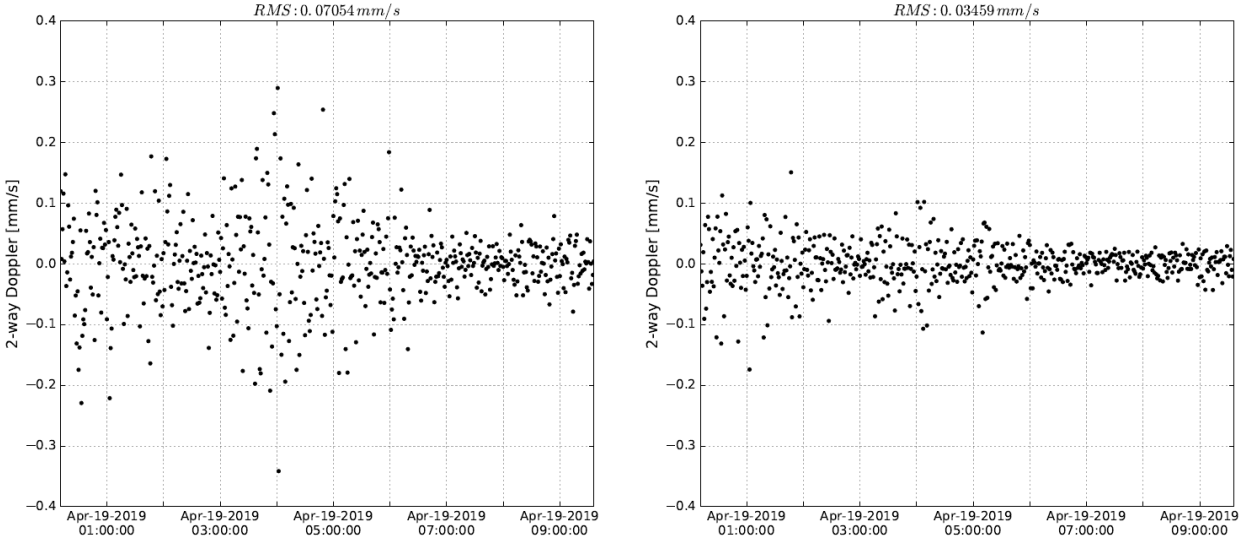

Figure 2 Comparison of Gaia Doppler residuals at 60 s count time for 19 April 2019. Left: using GNSS-based tropospheric calibrations; right: using TDCS-based calibrations, with 20 s integration time.

The left plot in Figure 3 shows a comparison of the ASD curves obtained by applying equation (6.1) to the Doppler residuals for four analyzed test cases, corresponding to GNSS calibrations, and TDCS calibrations at 1 s, 20 s, and 60 s integration time, respectively. Up to stability intervals of 10 s, all ASD curves, with the exception of the TDCS calibrations at 1 s integration time, are collapsed and approximately follow a power law with slope equal to -1. This behavior may suggest that the dominant error source at those characteristic timescales is the Doppler thermal noise (Iess, et al., 2014). However, for short integration times of the tropospheric products, the thermal noise of the MWR receiver components, which is introduced through the calibrations, becomes comparable in magnitude and induces the observed offset in the 1 s curve.

At longer stability intervals, the uncalibrated tropospheric delay becomes progressively more relevant, as indicated by the departure of all curves from the initial linear trend. From Figure 3 it is clear that the TDCS-based calibrations are able to capture the atmospheric variability along the slant path much better than their GNSS-based counterpart, with minimum ASD values that are obtained for a 20 s integration time of the ZWD, which is therefore used in the following sections for the overall performance characterization.

Similar results are observed through a comparison of the Power Spectral Density (PSD) of the Doppler residuals, which were generated using an adaptive Multi-Taper Spectral Estimation (MTSE) method (Percival & Walden, 1993). From the right plot of Figure 3 we can observe that most of the atmospheric instability that is calibrated using TDCS data occurs at characteristic frequencies lower than 10^{-2} Hz.

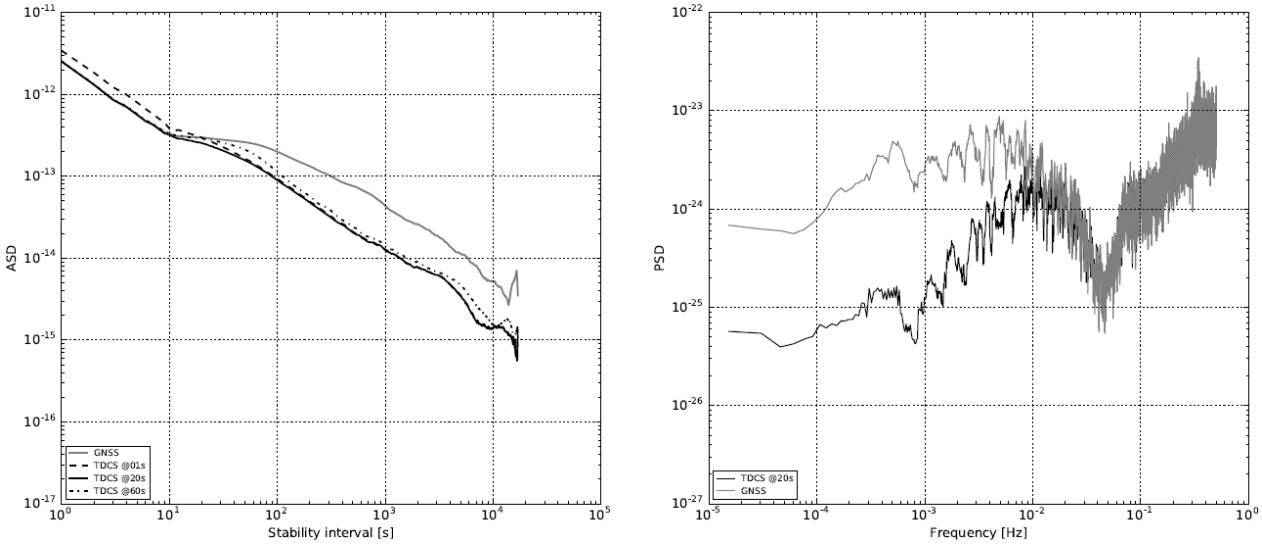

Figure 3 Left: ASD of Gaia Doppler residuals at 1 s count time for 19 April 2019. Four test cases are analyzed: a) GNSS calibrations (solid grey), b) TDCS calibrations at 1 s integration time (dashed black), c) TDCS calibrations at 20 s integration time (solid black), d) TDCS calibrations at 60 s integration time (dash-dotted black). Right: PSD of Gaia Doppler residuals at 1 s count time for 19 April 2019 (MTSE method). Only case a) and case c) are plotted here.

6.2 Overall statistics

The procedure described above was repeated for all the passes included within the OD analysis. Figure 4 compares the Doppler residuals at 60 s count time, using GNSS-based calibrations and TDCS-based calibration, respectively, for the whole testbed campaign. An overall improvement of the residuals is clearly detectable, and this is more pronounced depending on the atmospheric conditions encountered during the passes.

Figure 5, provides a comparison of the RMS values for the two analyzed cases. More specifically, the left plot depicts the absolute RMS values for the Doppler residuals as a function of the pass ID, while the right plot shows the ratio of the RMS values. The average noise reduction between the different tracking passes is approximately 34% when using TDCS-based calibrations instead of the GNSS-based ones, with a maximum reduction of 61% for pass 32 (18 July 2019). Although with different magnitudes, all passes show a noise reduction using TDCS calibrations, with the exception of pass 31 (16 July 2019) for which the noise is increased by approximately 11%. However, this pass incidentally coincides with a series of RCS and OTM maneuvers, which increase the number of estimated parameters and limit the availability of Doppler observables. Moreover, by looking at Table 1 we can observe that this pass corresponds to an extremely dry condition, thus reducing the actual signal-to-noise ratio of the estimated calibrations.

Considering the limited number of observed tracking passes, it is difficult to pinpoint an exact cause for the variability in performance of the TDCS products. The amount of uncalibrated atmospheric variability affecting the Doppler residuals depends both on the actual value of the integrated ZWD and on the accuracy of the calibrations, which strongly depends on the atmospheric conditions. Using TDCS calibrations may also introduce additional error sources such as the mechanical noise from wind-induced vibrations of the ATS mounting structure or radiometric retrieval errors induced by fast variations in the observed atmospheric scene (in particular at low elevations), which may dominate over the tropospheric noise for particular tracking passes.

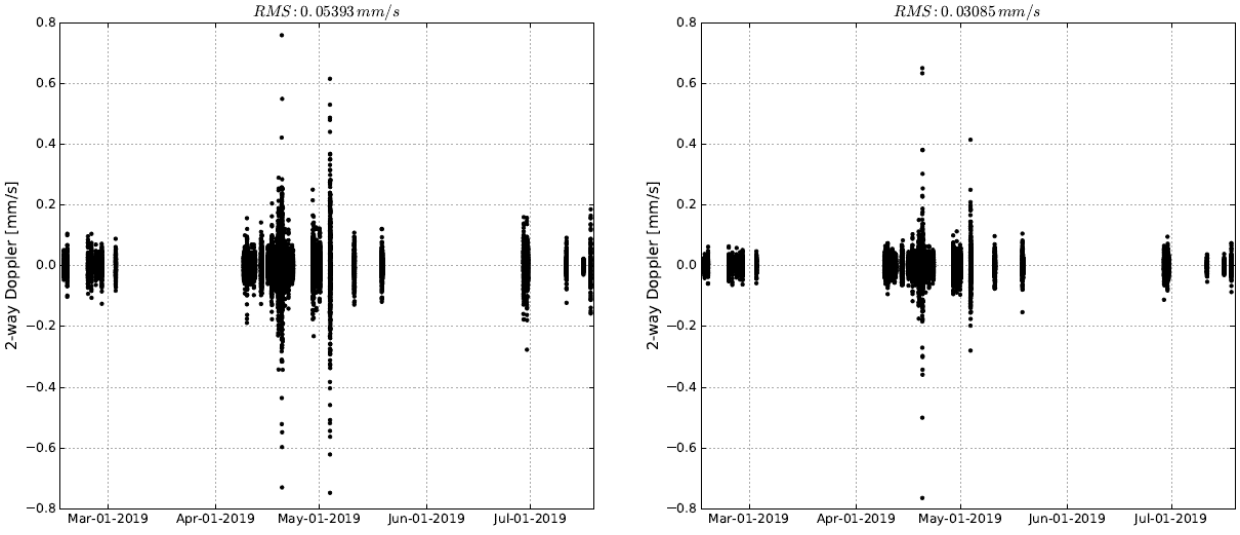

Figure 4 Comparison of Gaia Doppler residuals for the whole testbed campaign. Left: using GNSS-based tropospheric calibrations; right: using TDCS-based calibrations with 20 s integration time.

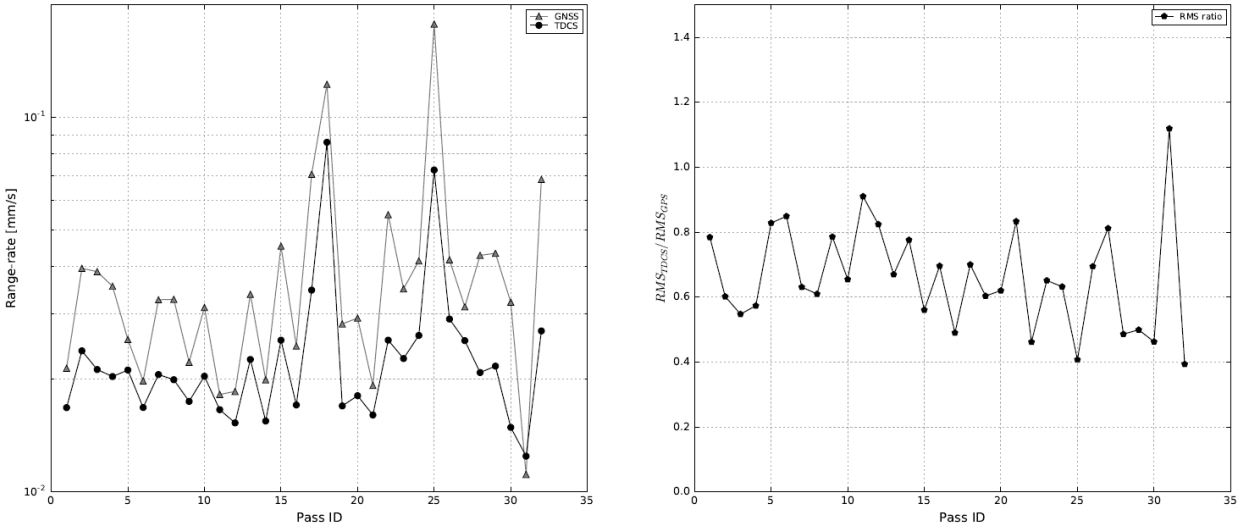

Figure 5 Left: absolute RMS values for the Doppler residuals at 60 s count time using GNSS-based calibrations (grey triangles) and TDCS-based calibrations with 20 s integration time (black circles); right: ratio between RMS values for the two test cases.

Finally, Figure 6 offers a comparison of the ASD curves computed at characteristic stability intervals of 20 s, 60 s, and 1000 s, respectively, which represent typical values used for radio science applications. It can be observed that both the 20 s and 60 s curves shows a consistent reduction of the ASD values when using TDCS-based calibrations, with a magnitude that is more pronounced for the latter case. A similar reduction is observed for the 1000 s stability interval curves, with the exception of a couple of tracking passes, corresponding to pass IDs 11 and 14. A detailed inspection of the Doppler residuals of these tracking passes highlighted the introduction by the TDCS calibrations of small wave-like signatures at elevation angles below 30°. The cause of these signatures, which is currently under investigation, is expected to be related to the granularity of the elevation-dependent retrieval coefficients. The retrieval-induced error, which is small for most of the tracking passes, may become relevant for specific atmospheric conditions and particularly at low elevation angles, for which the observed atmospheric scene may be subject to fast variations.

Additional investigations may be required for a fine-tuning of the retrieval algorithm, which could improve the accuracy of the tropospheric calibrations at low elevations.

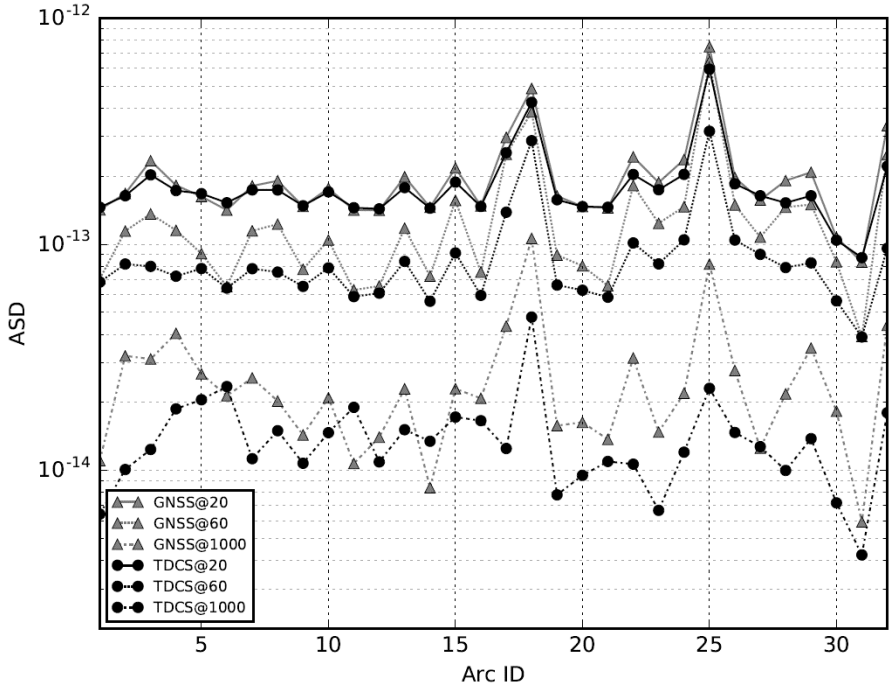

Figure 6 Comparison of ASD values for the Doppler residuals at 1 s count time. ASD values are displayed at characteristic stability intervals of 20 s (solid line), 60 s (dotted line), and 1000 s (dash-dotted line).

7 Conclusions

This work presented the first statistical characterization of the end-to-end performances of the TDCS prototype that was installed at ESA's DS3 station complex in Malargüe, Argentina.

An extensive testbed campaign was carried out between February and September 2019, using the TDCS alongside the main DSA to track the Gaia S/C during a series of scheduled passes. The described analysis, which does not replicate the full OD solution for the navigation of Gaia, was mostly intended as a side-by-side comparison of the OD performance when TDCS-based tropospheric calibrations are used in place of the standard GNSS-based calibrations.

The instrument performance was characterized in terms of RMS values of the Doppler residuals and ASD values of the fractional frequency stability computed at characteristic stability intervals. The OD results indicate that an average reduction of about 34% in the RMS of the Doppler residuals is observed when TDCS-based calibrations are used. The actual magnitude of this improvement strongly varies between the different tracking passes, with maximum reductions around 61% and a few cases with no appreciable improvement. The overall quality of TDCS calibrations depends on several factors, including: the magnitude of the actual tropospheric variability (which depends on the integrated water vapor content along the slant direction), the accuracy of the NN retrieval, and the magnitude of the additional error sources introduced by the calibration process.

A complete statistical characterization of the TDCS performances would require the analysis of a larger sample of tracking passes under diverse observing conditions.

Future work may therefore include additional observations for the Gaia S/C, along with the analysis of large datasets for BepiColombo, Mars Express, or the ExoMars orbiter, which are routinely being tracked from the DS3 station complex. More specifically, an analysis of BepiColombo tracking passes is currently underway as part of the cruise tests and solar conjunction radio science experiments. This analysis is expected to improve the TDCS

performance characterization, thanks to the more accurate K_a/K_a band tracking link that allows for an almost complete cancellation of the solar and ionospheric plasma noises. Moreover, most of these observations will occur during daytime as opposed to the more still and dry air conditions that were encountered for the Gaia night-time observations described in this paper, allowing to broaden the range of observing conditions for the performance characterization.

Acknowledgments, Samples, and Data

The research described in this paper was carried out at the University of Bologna in the framework of ESA contract No. 4000116932/16/NL/AF "Development of a Ground Tropospheric Media Calibration System for Accurate Ranging of Space Science Missions". The authors want to express their gratitude to the personnel involved in the TDCS project who gave precious suggestions for completing this study, and in particular, Alberto Graziani, and Guillaume Autret from the European Space Agency, the ESOC Flight Dynamics team and in particular Frank Budnik and Gabriele Bellei, Emiliano Orlandi and Harald Czekala from RPG for the retrieval development and tests, Danielle Vanhoenacker-Janvier and Laurent Quibus from Université Catholique de Louvain-la-Neuve, Belgium, and Gilles Mariotti from SITAEL S.p.A. RLM, MZ and PT wish to acknowledge Caltech and the Jet Propulsion Laboratory for granting the University of Bologna a license to an executable version of MONTE Project Edition S/W.
Data for this research are not publicly available due to ESA general contract conditions.
Upon acceptance of the manuscript, all relevant data will be stored in the Guest Storage Facility (GSF) within ESA's Planetary Science Archive (https://archives.esac.esa.int/psa/). Academic and research institutions can request a license to use the data for their own research scientific purposes without the right to grant sublicences.

8 References

Asmar, S., Armstrong, J., Iess, L., & Tortora, P. (2005, 4). Spacecraft Doppler tracking: Noise budget and accuracy achievable in precision radio science observations. *Radio Science, 40*(2). https://doi.org/10.1029/2004RS003101

Bertotti, B., Comoretto, G., & Iess, L. (1993). Doppler tracking of spacecraft with multi-frequency links. *Astronomy and Astrophysics*, 608-616.

Bierman, G. J. (2006). Factorization methods for discrete sequential estimation. Courier Corporation.

Cappuccio, P., Hickey, A., Durante, D., Di Benedetto, M., Iess, L., De Marchi, F., . . . Mura, A. (2020). Ganymede's gravity, tides and rotational state from JUICE's 3GM experiment simulation. *Planetary and Space Science, 187*, 104902. https://www.sciencedirect.com/science/article/pii/S003206331930385X

Casajus, L. G., Zannoni, M., Modenini, D., Tortora, P., Nimmo, F., Van Hoolst, T., ... & Oudrhiri, K. (2021). Updated Europa gravity field and interior structure from a reanalysis of Galileo tracking data. Icarus, 358, 114187.

Durante, D., Hemingway, D. J., Racioppa, P., Iess, L., & Stevenson, D. J. (2019). Titan's gravity field and interior structure after Cassini. Icarus, 326, 123-132.

Durante, D., Parisi, M., Serra, D., Zannoni, M., Notaro, V., Racioppa, P., . . . Iess, L. (2020). Jupiter's gravity field halfway through the Juno mission. *Geophysical Research Letters, 47*(4), 1-8.

Estefan, J., & Sovers, O. (1994). *A Comparative Survey of Current and Proposed Tropospheric Refraction-Delay Models for DSN Radio Metric Data Calibration.*

Evans, S., Taber, W., Drain, T., Smith, J., Wu, H.-C., Guevara, M., . . . Evans, J. (2018). MONTE: the next generation of mission design and navigation software. *CEAS Space Journal, 10*(1), 79-86. https://doi.org/10.1007/s12567-017-0171-7

Folkner, W., Williams, J., Boggs, D., Park, R., & Kuchynka, P. (2014). *The planetary and lunar ephemerides DE430 and DE431.* Interplanetary Network Progress Report 196(1).

Graziani, A., Jarlemark, P., Elgered, G., Martellucci, A., Mercolino, M., & Tortora, P. (2014). Assessment of Ground-Based Microwave Radiometry for Calibration of Atmospheric Variability in Spacecraft Tracking. *IEEE Transactions on Antennas and Propagation, 62*(5), 2634-2641.

Iess, Asmar, S. W., Cappuccio, P., Cascioli, G., De Marchi, F., di Stefano, I., . . . Zannoni, M. (2021). Gravity, Geodesy and Fundamental Physics with BepiColombo's MORE Investigation. *Space Science Reviews, 217*(1), 21. https://doi.org/10.1007/s11214-021-00800-3

Iess, L., Asmar, S., & Tortora, P. (2009). MORE: An advanced tracking experiment for the exploration of Mercury with the mission BepiColombo. *Acta Astronautica, 65*(5-6), 666-675.

Iess, L., Budnik, F., Colamarino, C., Corbelli, A., Di Benedetto, M., Fabbri, V., . . . Zannoni, M. (2012). ASTRA: Interdisciplinary study on enhancement of the end-to-end accuracy for spacecraft tracking techniques. *63rd International Astronautical Congress*, (pp. 1-11).

Iess, L., Di Benedetto, M., James, N., Mercolino, M., Simone, L., & Tortora, P. (2014). Astra: Interdisciplinary study on enhancement of the end-to-end accuracy for spacecraft tracking techniques. *Acta Astronautica, 94*(2), 699-707.

Jakowski, N., Hoque, M., & Mayer, C. (2011). A new global TEC model for estimating transionospheric radio wave propagation errors. *Journal of Geodesy, 85*(12), 965-974.

Keihm, S., & Marsh, K. (1998). New model-based Bayesian inversion algorithm for the retrieval of wet troposphere path delay from radiometric measurements. *Radio Science, 33*(2), 411-419.

Lasagni Manghi, R., Maschwitz, G., Tirtira, P., Rose, T., Martellucci, A., De Vicente, J., . . . Quibus, L. (2019). Tropospheric Delay Calibration System (TDCS): design and performances of a new generation of microwave radiomters for ESA deep space ground stations. *TT&C workshop.* Darmstadt.

Mariotti, G., & Tortora, P. (2013). Experimental validation of a dual uplink multifrequency dispersive noise calibration scheme for Deep Space tracking. *Radio Science, 48*(2), 111-117. https://doi.org/10.1002/rds.20024

Maschwitz, G., Czekala, H., Orlandi, E., & Rose, T. (2019). Accuracy and Performance of Atmospheric Delay by a RPG Microwave Radiometer With Respect to Ground Calibration Systems for ESA Radioscience. *TT&C workshop.* Darmstadt.

Molteni, F., Buizza, R., Palmer, T., & Petroliagis, T. (1996). The ECMWF ensemble prediction system: Methodology and validation. *Quarterly journal of the royal meteorological society, 122*(529), 73-119.

Naudet, C., Jacobs, C., Keihm, S., Lanyi, G., Linfield, R., Resch, G., . . . Tanner, A. (2000). The Media Calibration System for Cassini Radio Science: Part I. *The Telecommunications and Mission Operations Progress Report*, 42-123.

Niell, A. (1996). Global mapping functions for the atmosphere delay at radio wavelengths. *Journal of geophysical research: solid earth, 101*(B2), 3227-3246.

Percival, D., & Walden, A. (1993). *Spectral analysis for physical applications.* Cambridge University Press.

Quibus L. et al. Use and Accuracy of Numerical Weather Predictions to Support EM Wave Propagation Experiments, IEEE Transactions on Antennas and Propagation, vol. 67, No. 8, August 2019.

Resch, Clark, G., Keihm, J., Lanyi, S., Naudet, G., Riley, C., . . . Tanner, H. (2001). The media calibration system for Cassini radio science: Part II. *TMO Progress Report*, 42-145.

Ricart, M. (2018). TTCP Software Interface Control Document (ICD) for RM datasets, Issue 2.1.

Rose, T., Crewell, S, Löhnert, U., Simmer, C. (2005). A network suitable microwave radiometer for operational monitoring of the cloudy atmosphere. *Atmospheric Research, 75 (2005)*, 183-200.

Saastamoinen, J. (1972). Atmospheric Correction for the Troposphere and Stratosphere in Radio Ranging Satellites. In *The use of artificial satellites for geodesy* (pp. 247-251). American Geophysical Union (AGU). http://doi.wiley.com/10.1029/GM015p0247

Tanner, A. (1998). Development of a high-stability water vapor radiometer. *Radio Science, 33*(2), 449-462. https://doi.org/10.1029/97RS02749

Tanner, A., & Riley, A. (2003). Design and performance of a high-stability water vapor radiometer. *Radio Science, 38*(3). doi:https://doi.org/10.1029/2002RS002673

Thornton, C., & Border, J. (2003). *Radiometric Tracking Techniques for Deep-Space Navigation.* John Wiley & Sons.

Tortora, P., Iess, L., Bordi, J., Ekelund, J., & Roth, D. (2004). Precise Cassini navigation during solar conjunctions through multifrequency plasma calibrations. Journal of guidance, Control, and Dynamics, 27(2), 251-257.

Tortora, P., Crewell, S., Elgered, G., Graziani, A., Jarlemark, P., Loehnert, U., Martellucci A., Mercolino M., Rose T., and Schween, J. (2013). AWARDS: Advanced microwave radiometers for deep space stations. *Space Communications.*

Tortora, P., Zannoni, M., Hemingway, D., Nimmo, F., Jacobson, R. A., Iess, L., & Parisi, M. (2016). Rhea gravity field and interior modeling from Cassini data analysis. Icarus, 264, 264-273.

TRK-2-23 Media Calibration Interface. (2008). JPL.

Zannoni, M., & Tortora, P. (2013). Numerical error in interplanetary orbit determination software. Journal of Guidance, Control, and Dynamics, 36(4), 1008-1018.

Zannoni, M., Hemingway, D., Casajus, L. G., & Tortora, P. (2020). The gravity field and interior structure of Dione. Icarus, 345, 113713.